





# Joint Beam and Polarization Forming of Intelligent Reflecting Surfaces for Wireless Communications

Shinya Sugiura , Senior Member, IEEE, Yuto Kawai , Takayuki Matsui, Taehwa Lee , Member, IEEE, and Hideo Iizuka , Member, IEEE

**Abstract**—In this paper, we propose a novel intelligent reflecting surface (IRS) structure, which is capable of jointly forming desirable beam and polarization of a reflected wave with the aid of massive reflecting elements. More specifically, the proposed IRS is composed of unit cells, each having multiple variable capacitors. Active tuning of capacitances of the variable capacitors in each unit cell provides the full coverage of  $360^\circ$  in the reflection phase. Furthermore, polarization is switched from an incident wave to the reflected wave through the excitation of two orthogonal modes, enabling arbitrary phase distribution over the IRS for the desired polarization. As a result, the proposed IRS allows the increase of the signal-to-noise ratio (SNR) at the receiver in a communication scenario, by adjusting the reflection phase shift of each IRS element. Moreover, the reflection phase shifts of each IRS element are optimized with the aid of the Newton method, such that the received signal power of a receiver is maximized. In our simulations, it is demonstrated that our proposed IRS successfully maximizes the SNR at the receiver, both in the single-user and the broadcast multi-user scenarios, where multi-user interference is absent.

**Index Terms**—Beamforming, focusing, intelligent reflecting surface, large intelligent surface, massive MIMO, metasurface, polarization, reflection phase shift, wireless communication.

## I. INTRODUCTION

MASSIVE multiple-input multiple-output (MIMO) systems [1], [2] and relay-assisted cooperative communication schemes [3], [4] increase the available spatial degree of freedom in wireless communications, hence having the potential of boosting the information rate and reliability. Naturally, these benefits, owing to the co-located and distributed antenna arrays, are attained at the expense of the additional hardware cost, including multiple radio-frequency (RF) chains and terminals, as well as the associated increase of energy consumption.

Manuscript received October 8, 2020; revised December 22, 2020; accepted January 25, 2021. Date of publication January 28, 2021; date of current version March 10, 2021. The work of Shinya Sugiura was supported in part by the Japan Society for the Promotion of Science (JSPS) KAKENHI under Grants 16KK0120, 17H03259, and 17K18871 and in part by JST PRESTO under Grants JPMJPR1933. The review of this article was coordinated by Dr. B. Di. (Corresponding author: Shinya Sugiura.)

Shinya Sugiura is with the Institute of Industrial Science, The University of Tokyo, Tokyo 153-8505, Japan, and also with the Japan Science and Technology Agency (JST), Kawaguchi 332-0012, Japan (e-mail: sugiura@ieee.org).

Yuto Kawai is with the Institute of Industrial Science, The University of Tokyo, Tokyo 153-8505, Japan (e-mail: kawai-yuto888@g.ecc.u-tokyo.ac.jp).

Takayuki Matsui is with the Toyota Central R&D Labs., Inc., Nagakute, Aichi 480-1192, Japan (e-mail: t-matsui@mosk.tytlabs.co.jp).

Taehwa Lee and Hideo Iizuka are with the Toyota Research Institute of North America, Toyota Motor North America, Ann Arbor, MI 48105 USA (e-mail: taehwa.lee@toyota.com; hiizuka@mosk.tytlabs.co.jp).

Digital Object Identifier 10.1109/TVT.2021.3055237

To combat the limitations, intelligent reflecting surfaces (IRSs) have attracted much attention owing to the potential of practical implementation of beamforming with the aid of energy- and cost-effective massive reflecting elements [5]–[9].<sup>1</sup> Each element of an IRS is capable of electronically controlling the phase of the reflected electromagnetic waves, depending on the wireless environments from the transmitter and the receiver via the IRS. Two-dimensional thin structures of IRSs are readily installed on the walls of the building. Additionally, IRSs are cost-effective devices, which do not impose any substantial power consumption. This allows us to increase a signal-to-noise ratio (SNR) at the intended receiver while suppressing co-channel interference, hence significantly improving the achievable communication performance without relying on any additional transmit and receive antenna elements, as well as relay nodes. It is implied that IRSs constitute the MIMO function [1] in a virtual manner, where each element of an IRS can be regarded as an antenna element of a massive MIMO transmitter or as a relay node of an amplify-and-forward cooperative system. More specifically, IRSs were developed for the communication scenarios of both single-user [5], [12]–[16] and multi-user uplink [17], [18], as well as downlink scenarios [10], [19]. Furthermore, the IRSs were also considered for the use in the context of physical layer security [20]–[24], which can guarantee information theoretic security under the presence of an eavesdropper node. The concepts of the full-duplex communication and the simultaneous wireless information and power transfer were combined with the IRS in [25] and [26], respectively.

The implementation of IRSs typically relies on metasurfaces composed of unit cells, where fundamental functionalities in frequency, spatial direction, and polarization can be controlled [27]–[33]. In a reflecting metasurface, arbitrary phase profile can be distributed on the metasurface when each unit cell provides the full coverage of  $360^\circ$  in reflection phase. In a dynamic environment for wireless communication, unit cells in metasurfaces have to actively control both phase and polarization in reflected waves. Recently, active metasurfaces have been explored [34]–[40]. In [37], Dai *et al.* developed the 256-element IRS that combines the functions of phase shift and radiation together on each element of the IRS, where positive intrinsic-negative (PIN) diodes are used for configuring two-bit phase shifting. Also, in [38], Zhang *et al.* proposed a general

<sup>1</sup>IRSs are alternatively referred to as reconfigurable reflecting surfaces (RISs) [10] and large intelligent surfaces (LISs) [11], [12].

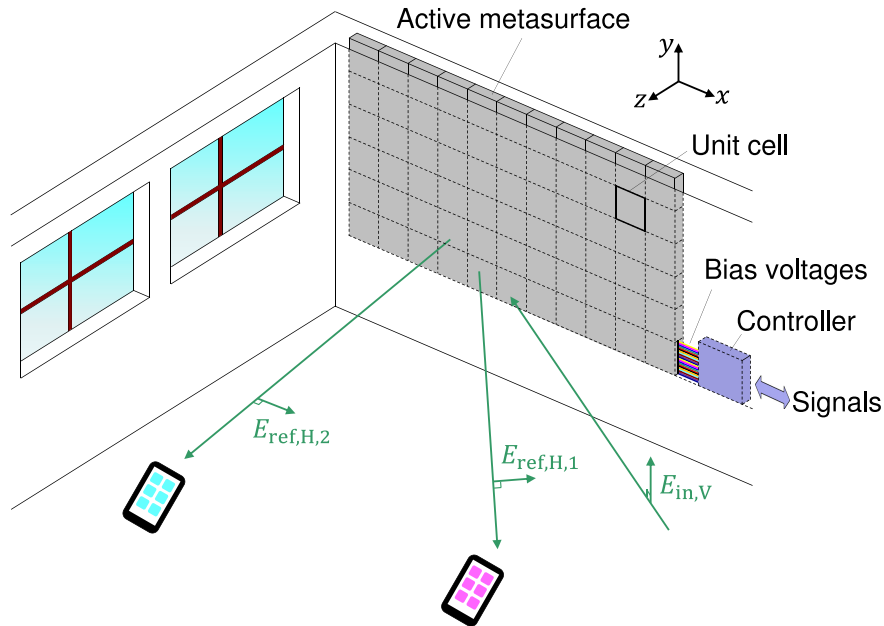


Fig. 1. Schematic illustration of a metasurface installed in a wall for redirecting an incoming wave to receivers.

theory of space-time modulated digital coding metasurfaces to obtain simultaneous manipulations of a reflected wave in both space and frequency dimensions. In [39], a programmable metasurface with dynamic polarization, scattering, and focusing control was proposed, where a unit element in the metasurface is integrated with a single PIN diode, such that a binary phase is encoded for a single polarization. Note that the metasurface developed in [39] only demonstrated a polarization switch from the normal incidence wave to the normal reflected wave, while the variation range of the reflection phase is limited in the unit cells. By contrast, a metasurface with variable-capacitor loading showed a dynamic control of the full coverage  $360^\circ$  in the reflection phase for a single polarization in [40]. Simultaneous active control of the beam direction and polarization is challenging for metasurfaces.

Against the background, the novel contributions of this paper are as follows. We propose a novel IRS structure, which is capable of jointly optimizing the beam and polarization of a reflected wave for wireless communications. More specifically, the proposed IRS is composed of unit cells, each having variable capacitors. Active tuning of the capacitances of the variable capacitors in each unit cell provides the full coverage of  $360^\circ$  in the reflection phase and polarization switch from an incident wave to the reflected wave through the excitation of two orthogonal modes. This enables arbitrary phase distribution over the IRS for the desired polarization. As a result, the proposed IRS allows the significant increase of the SNR at the receiver. The reflection phase shift of each IRS element is optimized with the aid of the quasi-Newton method in a numerical manner. Then, the capacitance settings of the variable capacitors are attained according to the optimized table that shows the relationship of reflection phase shifts and capacitances. In our simulations, it is demonstrated that our proposed scheme successfully maximizes

the SNR at the receiver in single-user unicast and multi-user broadcast scenarios.

The remainder of this paper is organized as follows. In Section II, we present the system model of the proposed system and IRS structure. In Section III, we provide our performance results. Finally, we conclude our paper in Section IV.

## II. INTELLIGENT REFLECTING SURFACES

We consider an IRS composed of unit cells, which may be installed in a wall, as shown in Fig. 1. Each unit cell can actively tune the phase and the polarization in reflection waves by variable capacitors. The IRS is desired to redirect an incident wave to receivers at an arbitrary position with arbitrary polarization. We assume an extreme case where the vertically polarized wave (the electric field is vertical) is incident on the IRS, and two receivers can receive horizontally polarized waves (the electric field is horizontal). Similar to the previous studies [5], [14], [16], [18], [19], a central coordinator controls the parameters of IRS elements under the assumption that the channel coefficients between the transmitter and the IRS elements, as well as those between the IRS elements and the receiver, are accurately acquired, for the sake of simplicity. The controller provides bias voltages to variable capacitors in each unit cell so that the IRS can redirect the vertically incident wave into the two receivers with the horizontal polarization. We present the configuration of our IRS in Section II-A. We show that unit cells of the IRS can efficiently switch the polarization from an incident wave to the reflected wave, and simultaneously provide the  $360^\circ$  full coverage of the reflection phase in Section II-B. The full coverage of the reflection phase is maintained in the case with

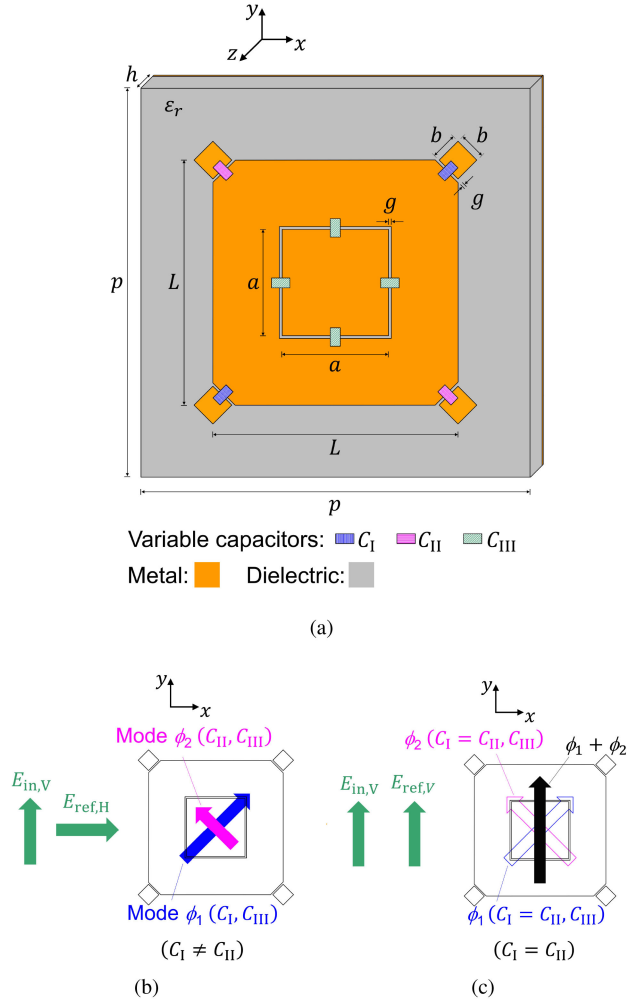


Fig. 2. (a) Geometry of a unit cell having two-fold rotational symmetry. Conductive patterns are printed on a dielectric substrate with the backside ground plane. Variable capacitors  $C_I$ ,  $C_{II}$ , and  $C_{III}$  are loaded on the conductive patterns. Parameters are  $p = 180$  mm,  $L = 46$  mm,  $a = 20$  mm,  $b = 5$  mm,  $g = 0.5$  mm,  $h = 10$  mm, and  $\epsilon_r = 6.7$ , which are fixed throughout the paper. The design frequency is 1 GHz. Capacitances of  $C_I$ ,  $C_{II}$ , and  $C_{III}$  are varied to control the polarization and the phase in reflected waves. (b) Two orthogonal modes  $\phi_1$  and  $\phi_2$  are excited to switch the polarization from an incident wave to the reflected wave ( $C_I \neq C_{II}$ ). (c) Single mode is excited for the same polarization in the incident and reflected waves ( $C_I = C_{II}$ ).

the same polarization for both incident and reflection waves in Section II-C.

#### A. Configuration of Unit Cell

Fig. 2(a) shows the configuration of the unit cell with the dimensions of  $p \times p$  in our IRS. Conductor patterns are formed on a dielectric substrate with a thickness of  $h$  having the backside ground plane. The conductor patterns include the inner square with  $a \times a$ , the outer ring with  $L \times L$ , and four small squares with  $b \times b$  at four corners of the outer ring. Two variable capacitors  $C_I$  are diagonally implemented; between the top right corner of the outer ring and the nearest small square, and between the bottom left corner of the outer ring and the nearest small square. Likewise, two variable capacitors  $C_{II}$  are implemented at the

positions rotated by  $90^\circ$  from the positions of  $C_I$ . Four variable capacitors  $C_{III}$  are implemented across a gap between the inner square and the outer ring. We use the dimensions of the unit cell in the caption of Fig. 2 throughout the paper. The relative permittivity of the dielectric substrate has  $\epsilon_r = 6.7$ , assuming a wall material [41]. We set the design frequency of 1 GHz. Assuming that receivers are placed some distance away from our IRS (neither extremely wide angle nor extremely close to the IRS), we select  $p = 180$  mm ( $0.6\lambda_0$ , where  $\lambda_0$  is the free space wavelength.) to focus electromagnetic waves on receivers. The intrinsic resonance frequency is around 1 GHz by selecting  $L = 46$  mm as a half guided-wavelength, which corresponds to the fundamental resonance length and the minimum size. We regard the conductor pattern area on the dielectric substrate backed by the ground plane in the unit cell as a resonator. Discrete modes, which correspond to electromagnetic field distributions satisfying the boundary condition [42], are excited in the resonator.  $a = 20$  mm maximizes the tuning range of resonance frequencies since the resonance paths of the two orthogonal modes can be effectively tuned.  $b = 5$  mm is a typical perturbation size [43], and  $g = 0.5$  mm is a typical gap size for mounting variable capacitors [44]. Since the thickness  $h = 10$  mm of the substrate is much smaller than the wavelength  $\lambda_0$ , two transverse magnetic modes are excited with negligible higher order modes. We note that those dimensions do not need to be accurately determined since variable capacitors can equivalently tune those dimensions.

In the rest of this paper, we refer to vertical polarization for the electric field along the  $y$  axis and horizontal polarization for the electric field parallel to the  $zx$  plane. A capacitor, in general, has the impedance of  $1/(j\omega C_i)$ , where  $\omega$  and  $C_i$  are the angular frequency and the capacitance, and the impedance, in principle, can be varied from zero to infinite depending on the capacitance. For example, for the capacitor  $C_I$  at the right top of the conductor pattern area, zero impedance corresponds to the electric connection of the top right corner of the outer ring to the nearest small square. Whereas infinite impedance corresponds to the open end of the top right corner of the outer ring, i.e., the absence of the nearest small square. Mode  $\phi_1$  is excited along the diagonal direction from the left bottom to the right top in the resonator, and thus mode  $\phi_1$  can have different resonance lengths. Proper choice of the capacitance of variable capacitor  $C_I$  can generate an intermediate state between the two extreme cases. As a result, the resonant length of  $\phi_1$  can be tuned by varying the capacitance of variable capacitor  $C_I$ . Likewise, the resonance length of mode  $\phi_2$ , which is orthogonal to mode  $\phi_1$ , can be tuned by  $C_{II}$ . It is known that an asymmetric geometrical perturbation such as corner-cut of a square microstrip patch or unequal crossed slots in a patch generates two orthogonal modes having slightly different resonance frequencies, and proper coupling between the two modes exhibit bandpass filtering with input and output ports being orthogonal [43], [45]. In the unit cell of Fig. 2(a), two orthogonal modes  $\phi_1$  and  $\phi_2$  having different frequencies can be excited with different capacitances of  $C_I$  and  $C_{II}$  in the symmetric geometry, enabling the polarization switch between an incoming wave (vertical polarization) and the reflected wave (horizontal polarization) (Fig. 2(b)). There are

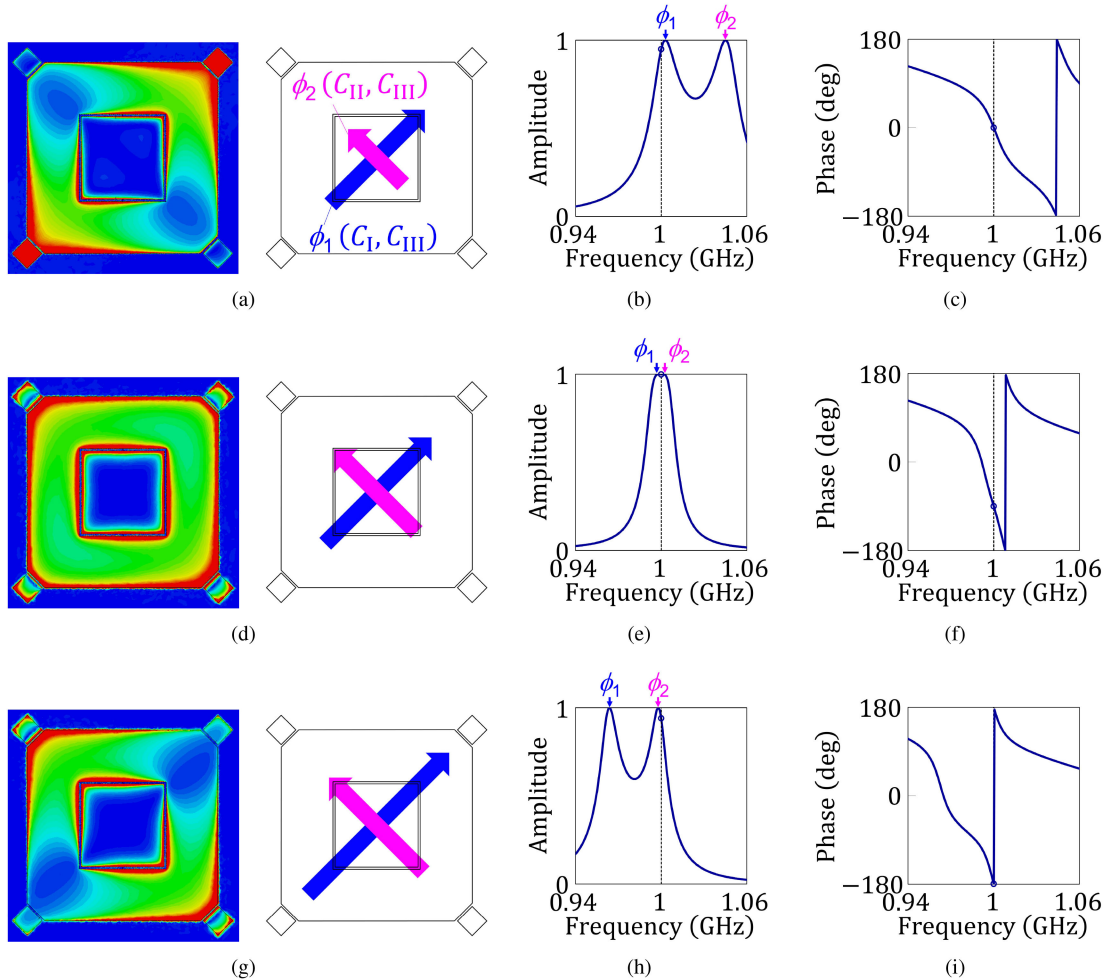


Fig. 3. Electric field distributions at 1 GHz (a), (d), (g), and frequency responses of reflection amplitudes (b), (e), (h), and phases (c), (f), (i), where the  $y$ -polarized wave is normally incident on the unit cell and the  $x$ -polarized reflection wave is calculated. Capacitances of variable capacitors ( $C_I$ ,  $C_{II}$ ,  $C_{III}$ ) have (100 pF, 0.1 pF, 0.9 pF) for (a), (b), (c), (0.7 pF, 0.1 pF, 2.58 pF) for (d), (e), (f), and (100 pF, 0.1 pF, 2.77 pF) for (g), (h), (i). Relative reflection phases have  $0^\circ$  in (c),  $-90^\circ$  in (f), and  $-179^\circ$  in (i) at 1 GHz.

two peaks in the reflection spectra, and variable capacitors  $C_I$  and  $C_{II}$  tune each of the two modes  $\phi_1$  and  $\phi_2$ , respectively, i.e., the peak-to-peak frequency difference.  $C_{III}$  tunes both frequencies of the two peaks since  $C_{III}$  can change the effective lengths of both modes. We note that the polarization conversion needs the difference of the resonance path lengths between the two modes. In other words, the two modes have different phases at the design frequency. When the two modes have the same resonance path length with the same capacitance of  $C_I$  and  $C_{III}$ , polarization conversion no longer occurs, and the polarization is maintained for an incoming and the reflected waves (Fig. 2(c)).

### B. Polarization Switchable IRS

We numerically investigate the unit cell of Fig. 2(a) by using the finite integration technique based simulator, CST Studio [46]. The vertically polarized wave is incident on the unit cell in the normal direction (along the  $-z$  direction), and the amplitude and the relative phase of the reflected wave are evaluated. Figs. 3(a)–3(i) show the electric field profiles, reflection

amplitude and reflection phase distributions for three different capacitance sets of  $C_I$ ,  $C_{II}$ , and  $C_{III}$ . Fig. 3(a) shows that the mode  $\phi_1$  is dominantly excited to have the electric field along the diagonal direction from the left bottom to the right top at low resonant frequency that coincides with the design frequency of 1 GHz by setting capacitances of ( $C_I$ ,  $C_{II}$ , and  $C_{III}$ ) as (100 pF, 0.1 pF, 0.9 pF). The amplitude and the relative reflection phase were 0.95 and  $0^\circ$  at 1 GHz, as shown in Figs. 3(b) and (c), respectively. When the capacitance set is ( $C_I$ ,  $C_{II}$ , and  $C_{III}$ ) = (0.7 pF, 0.1 pF, 2.58 pF), the frequencies of the two resonance peaks are close to each other, as shown in Fig. 3(e), and both the two modes  $\phi_1$  and  $\phi_2$  are excited at 1 GHz (Fig. 3(d)) with a relative reflection phase of  $-90^\circ$  (Fig. 3(f)) and an amplitude of 1 (Fig. 3(e)). Varying the capacitances of ( $C_I$ ,  $C_{II}$ , and  $C_{III}$ ) to (100 pF, 0.1 pF, 2.77 pF) then allows to coincide the high resonance frequency with 1 GHz with a  $-179^\circ$  reflection phase (Fig. 3(i)) and a 0.94 amplitude (Fig. 3(h)), where mode  $\phi_2$ , which is orthogonal to  $\phi_1$ , is dominantly excited, as shown in Fig. 3(g). We have assumed a range of 0.1 pF to 100 pF for capacitances of variable capacitors.

Next, we investigate the polarization conversion ratio (PCR) of the unit cell of Fig. 2, which is defined as

$$\text{PCR} = \left| \frac{E_{\text{ref,H}}}{E_{\text{in,V}}} \right| \quad (1)$$

where  $E_{\text{in,V}}$  and  $E_{\text{ref,H}}$  represent the vertical component of the incident electric field and the horizontal component of the reflected electric field, respectively. We note that in the lossless case with the incident wave of the vertical polarization, we have  $|E_{\text{ref,H}}|^2 + |E_{\text{ref,V}}|^2 = |E_{\text{in,V}}|^2$ , where the rest of the reflected wave has the vertical component  $E_{\text{in,V}}$  of the electric field.

In order to obtain highly efficient polarization conversion in the IRS, there are two requirements simultaneously satisfied, i.e., full coverage of  $360^\circ$  phase and high amplitude of the horizontally polarized reflection wave against the vertically polarized wave by using two modes  $\phi_1$  and  $\phi_2$ . In general, the reflection phase is widely varied around the resonance in a resonator, and thus we use the feature of the wide variation of the reflection phase around the resonance in our system. In addition, at least either  $\phi_1$  or  $\phi_2$  has a resonance peak around the design frequency of 1 GHz so that the horizontally polarized reflection wave can maintain high amplitude. We vary resonance frequencies of  $\phi_1$  (blue square) and  $\phi_2$  (pink diamonds), as shown in Fig. 4(a), while plotting the PCR in Fig. 4(b) and the associated capacitance set of ( $C_I$ ,  $C_{II}$ , and  $C_{III}$ ) in Fig. 4(c). Due to the two-fold rotational symmetry of the unit cell, resonance frequency of  $\phi_1$  and  $C_I$  at a relative reflection phase  $\xi$  have the same resonance frequency as  $\phi_2$  and the same capacitance as  $C_{II}$ , respectively, at the reflection phase of  $\xi \pm 180^\circ$ . Similarly, the PCR and  $C_{III}$  at a relative reflection phase  $\xi$  have the same PCR and the same capacitance at the reflection phase of  $\xi \pm 180^\circ$ . Around a reflection phase of  $\xi = -180^\circ$ ,  $\phi_2$  has a resonance frequency around 1 GHz, and  $\phi_1$  has low resonance frequency, which corresponds to Figs. 3(g)–(i). With the increase of  $\xi$ , the resonance frequency of  $\phi_1$  gets close to 1 GHz around  $90^\circ$  (Figs. 3(d)–(f)) while the resonance frequency of  $\phi_2$  has a small increase around 1 GHz. With further increase of  $\xi$ ,  $\phi_1$  has a resonance frequency around 1 GHz and the resonance frequency of  $\phi_2$  largely increases, with  $\xi = 0^\circ$  corresponding to Figs. 3(a)–(c). In the range of  $-180^\circ$  to  $0^\circ$  ( $0^\circ$  to  $180^\circ$ ),  $C_I$  ( $C_{II}$ ) and  $C_{III}$  are properly varied with  $C_{II}$  ( $C_I$ ) fixed. The behaviors of the capacitances can be understood from the relationship between the capacitance and the resonance frequency, i.e., small (large) capacitance  $C_i$  has large (small) impedance  $1/(\omega C_i)$ , and two conductor patterns via the variable capacitor is close to the open ends (electric connection). The resonance path length becomes short (long) and thus the resonance frequency increases (decreases). In the range of  $-180^\circ$  to  $0^\circ$ , the resonance frequency of mode  $\phi_2$  is tuned by  $C_{III}$  and the resonance frequency of mode  $\phi_1$  is tuned by  $C_I$  and  $C_{III}$ . As capacitance  $C_{III}$  has a small decrease from  $\xi = -180^\circ$  to  $\xi = -90^\circ$ , and largely decreases beyond  $\xi = -90^\circ$ , the resonance frequency of mode  $\phi_2$  has a small increase from  $\xi = -180^\circ$  to  $\xi = -90^\circ$ , and largely increases beyond  $\xi = -90^\circ$ , as mentioned above. Since the variation of  $C_{III}$  also affects the resonance frequency of mode  $\phi_1$ ,  $C_I$  is varied as shown in Fig. 3(c) to have the resonance frequency of mode  $\phi_1$  of Fig. 4(a). From this investigation, we observe that proper sets of

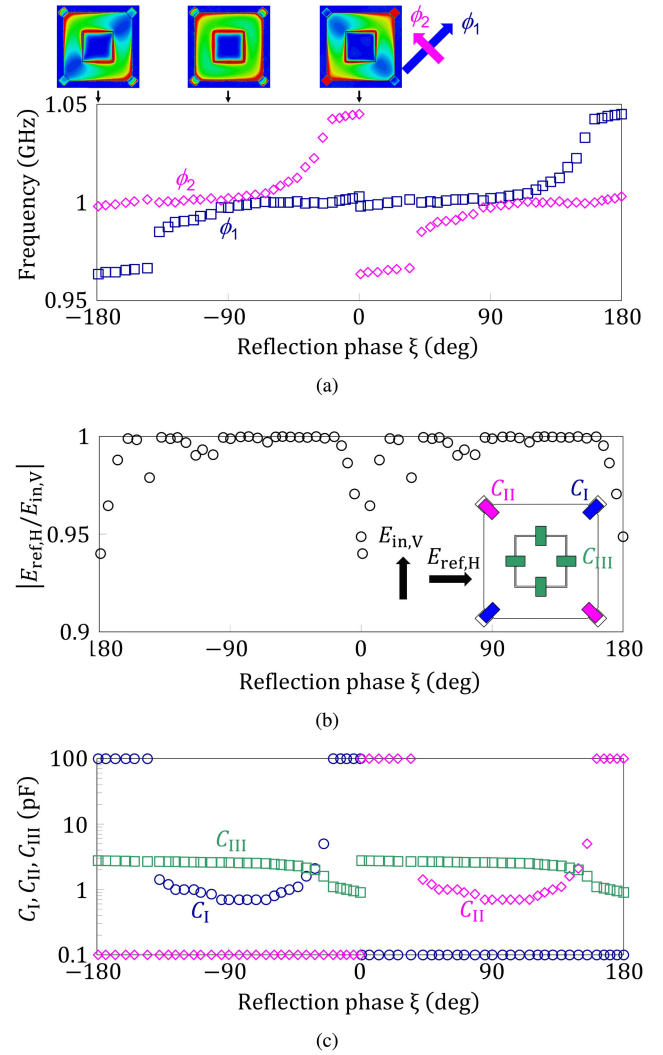


Fig. 4. (a) Resonance frequencies of two modes  $\phi_1$  (blue squares) and  $\phi_2$  (pink diamonds), PCR of the  $x$ -polarized reflected wave to the  $y$ -polarized incident wave, and (c) capacitances of variable capacitors  $C_I$ ,  $C_{II}$ , and  $C_{III}$  as a function of the reflection phase. Reflection phases in Fig. 3 are indicated by the arrows and the corresponding electric field distributions.

capacitances of ( $C_I$ ,  $C_{II}$ , and  $C_{III}$ ) exhibit the full coverage of  $360^\circ$  in the reflection phase and high efficiency of the polarization switch ( $> 0.94$ ). Therefore, arbitrary phase distribution can be achievable while maintaining a high efficiently and a desired polarization of a reflected wave.

### C. Polarization Maintained IRS

When a single-mode is excited in the unit cell by setting the same capacitance of  $C_I$  as  $C_{II}$  as shown in Fig. 5(a), an incident wave and the reflected wave have the same polarization. In this case, the restriction for capacitance variation is relaxed to meet the full coverage of  $360^\circ$  in the reflection phase, comparing with the polarization-switchable case, i.e., there are various sets of capacitances. A typical capacitance variation set is shown in Fig. 5(b). The unit cell of our IRS provides the full  $360^\circ$  in the relative reflection phase. We note that the unit cell has a unity reflection amplitude due to the assumption of lossless materials.

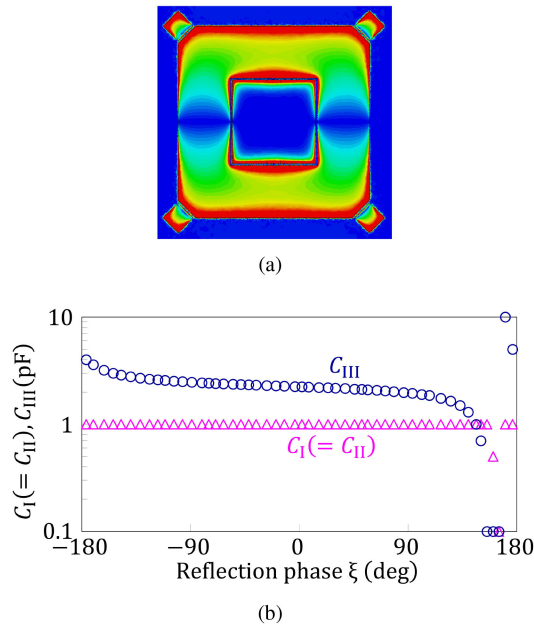


Fig. 5. (a) Electric field distribution and (b) capacitances of variable capacitors  $C_I (= C_{II})$  (pink triangles) and  $C_{III}$  (blue circles) as a function of the relative reflection phase for the case where both the incident wave and the reflected wave have the same polarization.

### III. PERFORMANCE RESULTS

In this section, we provide our performance results in order to characterize the capability of the proposed IRS-assisted wireless communication systems. The proposed IRS consists of  $11 \times 3$  unit cells, each having a size of  $180 \times 180 \text{ mm}^2$ , assuming the installation on a wall, i.e., the  $z = 0$  plane with other five planes being open boundaries, as shown in Figs. 6(a) and 6(b). Hence, the IRS size is set to  $W_m \times L_m = 1980 \times 540 \text{ mm}^2$ . A single transmit dipole antenna is positioned at  $(x, y, z) = (0 \text{ m}, 0 \text{ m}, 1.8 \text{ m})$ , which is vertically polarized along the  $y$  axis. These dimensions are used to validate the fundamental performance of our IRS. Moreover, we considered the frequency of 1 GHz.

According to the unit cell data sets in Section II-B, we numerically investigated the performance of a polarization-switchable IRS for both the single-receiver and two-receiver broadcast scenarios. IRSs for the same polarization case have been well explored in [34]–[40], and thus we do not investigate the polarization-maintained IRS. For the issue of channel estimation of all involved channel coefficients, refer to [8], [47].

Note that in our simulations, we assume that the parameters of the IRS were optimized based on the positions of the transmitter and the receiver or on the angles from the IRS to the transmitter and the receiver. However, in a multipath-rich scenario, channel state information between the transmitter and the IRS, as well as that between the IRS and the receiver, is required for optimizing the IRS parameters, similar to many previous IRS studies.

#### A. Single Receiver Scenario

Let us first consider an indoor point-to-point communication scenario. As shown in Figs. 6(a) and 6(b), the feed

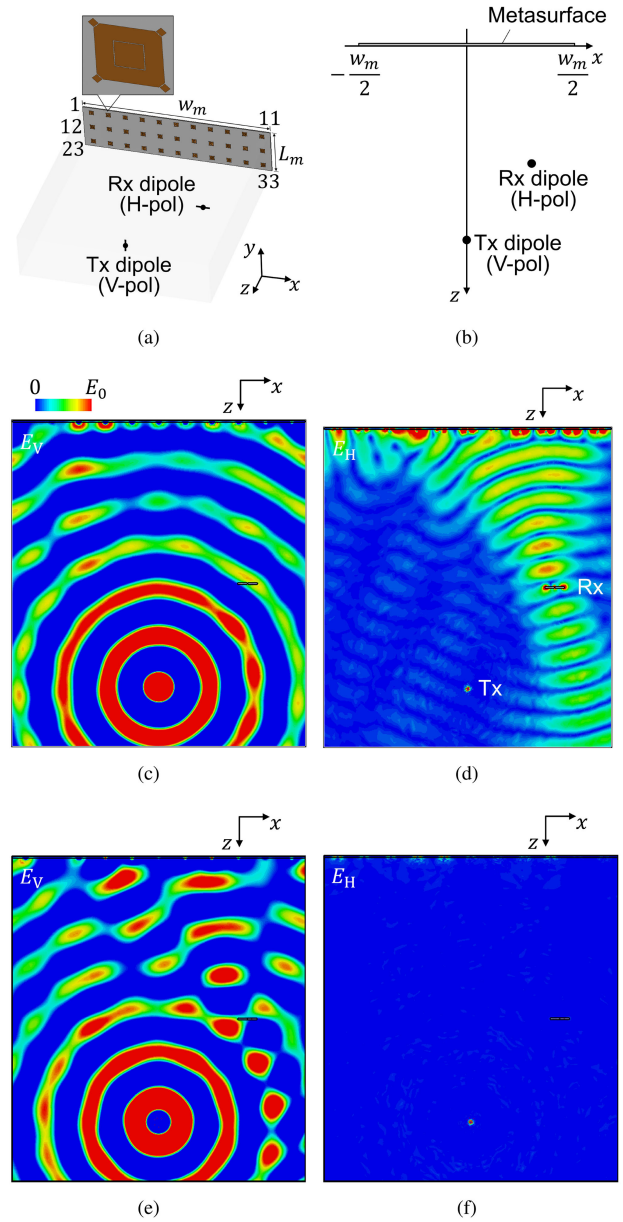


Fig. 6. Beam- and polarization-forming in a single receiver scenario of the proposed IRS system. (a) Perspective view of the system consisting of the proposed IRS having 3 by 11 unit cells, a vertically polarized transmit dipole antenna, and horizontally polarized receive dipole antenna, and (b) their placements in the  $xz$  plane at  $y = 0$ . Each of dipoles consists of a conductive cylinder having a length of 132 mm and a radius of 5 mm. In the rest of the paper, the transmit and the receive dipole antennas are placed at  $(x, y, z) = (0 \text{ m}, 0 \text{ m}, 1.8 \text{ m})$  and  $(0.6 \text{ m}, 0 \text{ m}, 1.1 \text{ m})$ , respectively. (c)–(f) Electric field distributions for (c), (e) the vertical polarization and (d), (f) the horizontal polarization in the  $xz$  plane at  $y = 0$  when capacitances of variable capacitors over the IRS are set to switch the polarization for (c), (d) or to have the same phase distribution over the IRS but no polarization switch as the counter system for (e), (f).

point of a receive dipole antenna is situated at  $(x, y, z) = (0.6 \text{ m}, 0 \text{ m}, 1.1 \text{ m})$ , which is horizontally polarized along the  $x$ -axis.

In order to maximize the received signal power, the parameters, i.e., the capacitances of the variable capacitors of each IRS element, are optimized. More specifically, we first estimate the optimized reflection phase shifts based on the wave propagation

paths between the transmit and receive antennas via the IRS. Here, the phase shift of the wave propagation path from the center of the  $i$ th IRS element to the feed point of the received antenna element is defined as  $\theta_i$  [deg.]. Similarly, the phase shift of the wave propagation path from the feed point of the transmit antenna element to the center of the  $i$ th element is given by  $\zeta_i$  [deg.]. Note that  $\theta_i$  and  $\zeta_i$  are determined uniquely by the system configuration, regardless of the variable capacitor values. By defining the reflection phase shift of the  $i$ th IRS element as  $\xi_i$  [deg.], the optimized reflection phase shifts  $\hat{\xi} = [\hat{\xi}_1, \dots, \hat{\xi}_{33}]$  are given by solving the following problem:

$$\hat{\xi} = \arg \max_{\xi} \left| \sum_{i=1}^{33} \text{PCR}_i \exp \left\{ j(\zeta_i + \xi_i + \theta_i) \frac{\pi}{180^\circ} \right\} \right|, \quad (2)$$

where we have  $\xi = [\xi_1, \dots, \xi_{33}]$ , and  $\text{PCR}_i$  represents the PCR of the  $i$ th IRS element. For the sake of simplicity, we set  $\text{PCR}_i = 1$  in our optimization of (2). Note that this assumption was validated by a high polarization efficiency regardless of the reflection phase shift, as shown in Fig. 4(b).

The solution of (2) was numerically attained by the quasi-Newton method [48]. More specifically, in each Monte Carlo simulation, the quasi-Newton method was carried out by randomly generating the initial values for  $\hat{\xi}$ . Then, after a sufficient number of Monte Carlo simulations, the  $\hat{\xi}$  values corresponding to the highest cost function was obtained as the solution. By denoting the number of Monte Carlo simulations, that of iterations in the quasi-Newton method, and that of the IRS elements as  $I_{\text{MC}}$ ,  $I_{\text{Newton}}$ , and  $K$ , respectively, the associated complexity order is given by  $\mathcal{O}(I_{\text{MC}} I_{\text{Newton}} K^2)$ . In our extensive simulations, the convergence was typically attained with  $I_{\text{MC}} \leq 100$  and  $I_{\text{Newton}} \leq 10$ .

Furthermore, these reflection phase shifts  $\hat{\xi}$  were used for obtaining the optimized variable capacitor values of the  $i$ th IRS element  $C_{\text{I}}^{(i)}, C_{\text{II}}^{(i)}, C_{\text{III}}^{(i)}$ , according to Fig. 4(c).

In order to validate our parameter optimization, we carried out full-dimensional electromagnetic simulations with the aid of CST Studio [46]. Figs. 6(c) and 6(d) show the resultant distributions of vertical and horizontal electric fields. As shown in Fig. 6(c), the proposed IRS did not reflect the vertically-polarized electromagnetic wave, since the IRS parameters were optimized so that the reflected waves became horizontally polarized. Furthermore, observe in Fig. 6(d) that the horizontally-polarized wave was successfully focused on the received antenna element. This implies that as the explicit benefits of our IRS that can simultaneously optimize the beam and polarization of a reflected wave, the received signals attained a significantly high SNR. To provide further insights, the distributions of vertical and horizontal electric fields of the conventional IRS benchmark were shown in Figs. 6(e) and 6(f), where the polarization of a reflected wave remains unchanged by setting the capacitances of the IRS so as to have the same phase distribution but no polarization switch. Observe in Fig. 6(f) that vertical electric fields for both incident and reflected waves in each unit cell, the horizontal electric fields of the reflected waves were negligibly small, and the associated power at the horizontally polarized received dipole antenna was less than  $-65$  dB.

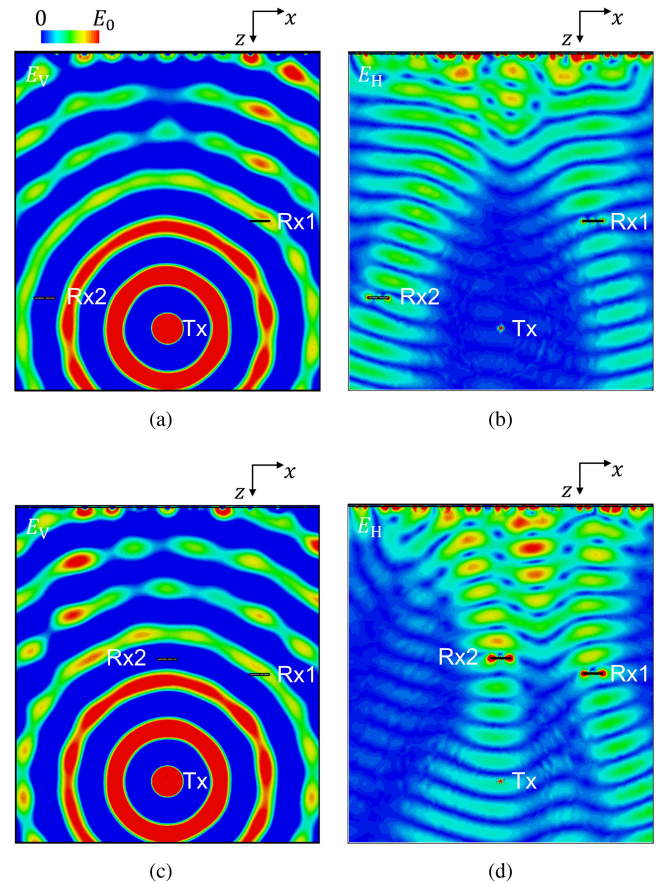


Fig. 7. Beam- and polarization-forming in two-receiver broadcast scenarios of the proposed IRS system. The second receive dipole antenna is additionally placed at  $(x, y, z) = (-0.8 \text{ m}, 0 \text{ m}, 1.6 \text{ m})$  for (a) the vertical polarization and (b) the horizontal polarization, as well as at  $(0 \text{ m}, 0 \text{ m}, 1 \text{ m})$  for (c) the vertical polarization and (d) the horizontal polarization in the system of Fig. 6.

## B. Two-Receiver Broadcast Scenario

Next, we consider the two-receiver broadcast scenario, where the same information is transmitted to both the receivers, hence absent of interference. We assume that both the receive antennas are horizontally polarized along the  $x$ -axis, similar to the single-receiver scenario of Section III-A.

Let us define the reflection phase shift of the wave propagation path from the center of  $i$ th IRS element to the antenna element of the  $k$ th receiver as  $\theta_i^{(k)}$ . Then, in order to attain the optimized reflection phase shifts, the following problem is considered:

$$\hat{\xi} = \arg \max_{\xi} \min \left[ \left| \sum_{i=1}^{33} \exp \left\{ j(\zeta_i + \xi_i + \theta_i^{(1)}) \frac{\pi}{180^\circ} \right\} \right|, \left| \sum_{i=1}^{33} \exp \left\{ j(\zeta_i + \xi_i + \theta_i^{(2)}) \frac{\pi}{180^\circ} \right\} \right| \right]. \quad (3)$$

The criterion of (3) is based on the maximization of a lower SNR, which is designed for guaranteeing high SNRs at the both receivers.

Figs. 7(a) and 7(b) show the distributions of the vertically- and horizontally-polarized electric fields for the scenarios where the antenna positions of the second receiver were set to

TABLE I  
SCATTERING PARAMETERS IN THE SYSTEMS OF FIGS. 6 AND 7

	Fig. 6	Figs. 7(a) and (b)	Figs. 7(c) and (d)
$\ S_{\text{Tx} \rightarrow \text{Rx1}}\ $	-28.2 dB	-32.7 dB	-31.2 dB
$\ S_{\text{Tx} \rightarrow \text{Rx2}}\ $	—	-31.6 dB	-29.9 dB

$(x, y, z) = (-0.8 \text{ m}, 0 \text{ m}, 1.6 \text{ m})$ , respectively, while Figs. 7(c) and 7(d) show those of  $(0 \text{ m}, 0 \text{ m}, 1 \text{ m})$ , respectively. The position of the first receiver was maintained to be the same as that employed in Fig. 6. Observe in Fig. 7 that the reflected beams were successfully oriented to both the receivers with the horizontal polarization in both the scenarios. Table I summarizes the scattering parameters from the transmitter to the receiver(s) in the systems of Figs. 6 and 7. It is quantitatively observed that received powers are enhanced for both the receivers.<sup>2</sup>

To elaborate a little further, while the reflection phase shifts were optimized for the two-receiver broadcast scenario, the same approach is readily applicable to the two-receiver multicast scenario by employing a specific multiple access scheme, such as time-domain multiple access, orthogonal frequency-domain multiple access, and non-orthogonal multiple access. Alternatively, it is possible to switch a beam- and polarization-pattern for each user for the sake of suppressing interference.

In this paper, we considered the range of 0.1 pF to 100 pF for capacitances of variable capacitors, and the capacitance range can be narrowed by further evaluating performance without serious degradation of wave-front control. A single variable capacitor, i.e., a varactor, in Fig. 2(a) can be composed of plural variable-capacitors to extend the capacitance range, similar to [44]. In [44], [49], variable capacitors were loaded in printed antennas without a ground plane, and no degradation was observed in radiation characteristics. Our IRS has a ground plane, and a bias circuit on the side of the ground plane may be less complex, comparing with antennas having no ground plane. Furthermore, varactors are diodes that are reversely biased by direct current (DC) voltages, and negligible DC flow and negligible power is dissipated. Hence the high power efficiency of IRSs remains attainable in our system.

We consider the material loss effect on the performance of our IRS. A copper loss of  $\sigma = 5.8 \times 10^7 \text{ S/m}$  is included in the metallic patterns, and the imaginary part is varied with the fixed real part of 6.7 in the dielectric permittivity  $\epsilon_r$ . Fig. 8(a) shows the received power of the horizontal receive dipole in the system of Fig. 6 with respect to the lossless case with -28.2 dB. When the copper loss is included (zero imaginary part of  $\epsilon_r$ ), the received power is decreased by 0.8 dB. As the loss of the dielectric material increases, the received power monotonically decreases. To understand the phenomenon in detail, we investigate the unit cell having variable capacitors of  $(C_I, C_{II}, C_{III}) = (100 \text{ pF}, 0.1 \text{ pF}, 0.9 \text{ pF})$ , which corresponds to (Figs. 3(a)–(c)) as a typical unit cell property. As the loss of the dielectric material increases, the horizontally polarized

<sup>2</sup>Additionally, we carried out the simulations of the conventional IRS benchmark scheme, which can only control the reflected beam. As a result, all the received amplitudes of the benchmark scheme, corresponding to Table I were more than 30 dB lower than those of the proposed IRS scheme, which is capable of simultaneously controlling both the beam and the polarization.

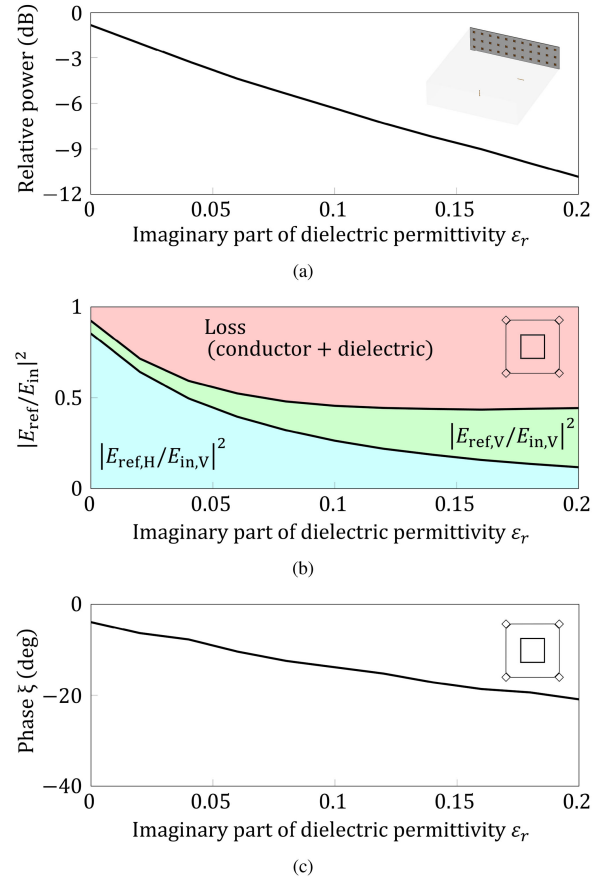


Fig. 8. Material loss effect on the performance of the IRS. A copper loss of  $\sigma = 5.8 \times 10^7 \text{ S/m}$  is included in the metallic patterns, and the imaginary part of the permittivity is varied with the fixed real value of 6.7 in the dielectric permittivity. (a) Relative power  $|S_{\text{Tx} \rightarrow \text{Rx1}}|$  of the receiving antenna in the system of Fig. 6 with respect to the lossless case with -28.2 dB. (b) Reflection power and (c) phase of the unit cell having the variable capacitance set of  $(C_I, C_{II}, C_{III}) = (100 \text{ pF}, 0.1 \text{ pF}, 0.9 \text{ pF})$  (Figs. 3(a)–(c)).

reflection wave  $|E_{\text{ref,H}}/E_{\text{in,V}}|$  decreases with the vertically polarized incidence wave, as expected. Interestingly, the vertically polarized reflection wave  $|E_{\text{ref,V}}/E_{\text{in,V}}|$  increases with the increase of the material loss in our IRS. The reflection phase is varied by  $20^\circ$  in the range of the plot (Fig. 8(c)).

#### IV. CONCLUSION

In this paper, we proposed the novel IRS-based wireless communication system, which is capable of adapting reflected beam and polarization in a simultaneous manner. Loading variable capacitors in each unit cell of the IRS allows us to dynamically tune each of the resonance frequencies of the two orthogonal modes. Proper capacitance sets provided the full coverage  $360^\circ$  of the reflection phase and polarization switch with an efficiency higher than 94% in unit cells, enabling arbitrary phase distribution over the IRS for the desired polarization. In our single-receiver and two-receiver broadcast scenarios, we derived and solved the optimization problems, in order to achieve the reflection phase shift sets at the IRS elements. It was demonstrated that our scheme successfully focused the transmit energies on the receivers via the IRS with the designed polarization.



## REFERENCES

- [1] E. G. Larsson, O. Edfors, F. Tufvesson, and T. L. Marzetta, "Massive MIMO for next generation wireless systems," *IEEE Commun. Mag.*, vol. 52, no. 2, pp. 186–195, Feb. 2014.
- [2] M. Di Renzo, H. Haas, A. Ghrayeb, S. Sugiura, and L. Hanzo, "Spatial modulation for generalized MIMO: Challenges, opportunities, and implementation," *IEEE Proc. IRE*, vol. 102, no. 1, pp. 56–103, Jan. 2014.
- [3] Y. Jing and H. Jafarkhani, "Single and multiple relay selection schemes and their achievable diversity orders," *IEEE Trans. Wireless Commun.*, vol. 8, no. 3, pp. 1414–1423, Mar. 2009.
- [4] S. Sugiura, S. X. Ng, L. Kong, S. Chen, and L. Hanzo, "Quasi-synchronous cooperative networks: A practical cooperative transmission protocol," *IEEE Veh. Technol. Mag.*, vol. 7, no. 4, pp. 66–76, Dec. 2012.
- [5] Q. Wu and R. Zhang, "Intelligent reflecting surface enhanced wireless network via joint active and passive beamforming," *IEEE Trans. Wireless Commun.*, vol. 18, no. 11, pp. 5394–5409, Nov. 2019.
- [6] M. Di Renzo *et al.*, "Smart radio environments empowered by reconfigurable AI meta-surfaces: An idea whose time has come," *EURASIP J. Wireless Commun. Netw.*, vol. 2019, no. 1, pp. 1–20, May 2019.
- [7] O. Özdoğan, E. Björnson, and E. G. Larsson, "Intelligent reflecting surfaces: Physics, propagation, and pathloss modeling," *IEEE Wireless Commun. Lett.*, vol. 9, no. 5, pp. 581–585, May 2020.
- [8] Q. Wu and R. Zhang, "Towards smart and reconfigurable environment: Intelligent reflecting surface aided wireless network," *IEEE Commun. Mag.*, vol. 58, no. 1, pp. 106–112, Jan. 2020.
- [9] M. Di Renzo *et al.*, "Reconfigurable intelligent surfaces vs. relaying: Differences, similarities, and performance comparison," *IEEE Open J. Commun. Soc.*, vol. 1, pp. 798–807, 2020.
- [10] Q. Nadeem, A. Kammoun, A. Chaaban, M. Debbah, and M. Alouini, "Asymptotic max-min SINR analysis of reconfigurable intelligent surface assisted MISO systems," *IEEE Trans. Wireless Commun.*, vol. 19, no. 12, pp. 7748–7764, Dec. 2020.
- [11] S. Hu, F. Rusek, and O. Edfors, "Beyond massive MIMO: The potential of data transmission with large intelligent surfaces," *IEEE Trans. Signal Process.*, vol. 66, no. 10, pp. 2746–2758, May 2018.
- [12] Y. Han, W. Tang, S. Jin, C. Wen, and X. Ma, "Large intelligent surface-assisted wireless communication exploiting statistical CSI," *IEEE Trans. Veh. Technol.*, vol. 68, no. 8, pp. 8238–8242, Aug. 2019.
- [13] X. Tan, Z. Sun, D. Koutsonikolas, and J. M. Jornet, "Enabling indoor mobile millimeter-wave networks based on smart reflect-arrays," in *Proc. IEEE INFOCOM*, Honolulu, HI, USA, Apr. 2018, pp. 270–278.
- [14] Q. Wu and R. Zhang, "Beamforming optimization for wireless network aided by intelligent reflecting surface with discrete phase shifts," *IEEE Trans. Commun.*, vol. 68, no. 3, pp. 1838–1851, Mar. 2020.
- [15] H. Zhang, B. Di, L. Song, and Z. Han, "Reconfigurable intelligent surfaces assisted communications with limited phase shifts: How many phase shifts are enough?," *IEEE Trans. Veh. Technol.*, vol. 69, no. 4, pp. 4498–4502, Apr. 2020.
- [16] J. Ye, S. Guo, and M. Alouini, "Joint reflecting and precoding designs for SER minimization in reconfigurable intelligent surfaces assisted MIMO systems," *IEEE Trans. Wireless Commun.*, vol. 19, no. 8, pp. 5561–5574, Aug. 2020.
- [17] M. Jung, W. Saad, Y. Jang, G. Kong, and S. Choi, "Performance analysis of large intelligent surfaces (LISs): Asymptotic data rate and channel hardening effects," *IEEE Trans. Wireless Commun.*, vol. 19, no. 3, pp. 2052–2065, Mar. 2020.
- [18] W. Yan, X. Yuan, Z. He, and X. Kuai, "Passive beamforming and information transfer design for reconfigurable intelligent surfaces aided multiuser MIMO systems," *IEEE J. Sel. Areas Commun.*, vol. 38, no. 8, pp. 1793–1808, Aug. 2020.
- [19] C. Huang, A. Zappone, G. C. Alexandropoulos, M. Debbah, and C. Yuen, "Reconfigurable intelligent surfaces for energy efficiency in wireless communication," *IEEE Trans. Wireless Commun.*, vol. 18, no. 8, pp. 4157–4170, Aug. 2019.
- [20] J. Chen, Y. Liang, Y. Pei, and H. Guo, "Intelligent reflecting surface: A programmable wireless environment for physical layer security," *IEEE Access*, vol. 7, pp. 82 599–82 612, 2019.
- [21] X. Yu, D. Xu, and R. Schober, "Enabling secure wireless communications via intelligent reflecting surfaces," in *Proc. IEEE Glob. Commun. Conf.*, Waikoloa, HI, USA, Dec. 2019, pp. 1–6.
- [22] H. Shen, W. Xu, S. Gong, Z. He, and C. Zhao, "Secrecy rate maximization for intelligent reflecting surface assisted multi-antenna communications," *IEEE Commun. Lett.*, vol. 23, no. 9, pp. 1488–1492, Sep. 2019.
- [23] X. Guan, Q. Wu, and R. Zhang, "Intelligent reflecting surface assisted secrecy communication: Is artificial noise helpful or not?," *IEEE Wireless Commun. Lett.*, vol. 9, no. 6, pp. 778–782, Jun. 2020.
- [24] L. Dong and H. Wang, "Secure MIMO transmission via intelligent reflecting surface," *IEEE Wireless Commun. Lett.*, vol. 9, no. 6, pp. 787–790, Jun. 2020.
- [25] H. Shen, T. Ding, W. Xu, and C. Zhao, "Beamforming design with fast convergence for IRS-aided full-duplex communication," *IEEE Commun. Lett.*, vol. 24, no. 12, pp. 2849–2853, Dec. 2020.
- [26] Q. Wu and R. Zhang, "Weighted sum power maximization for intelligent reflecting surface aided SWIPT," *IEEE Wireless Commun. Lett.*, vol. 9, no. 5, pp. 586–590, May 2020.
- [27] C. Pfeiffer and A. Grbic, "Metamaterial Huygens' surfaces: Tailoring wave fronts with reflectionless sheets," *Phys. Rev. Lett.*, vol. 110, no. 19, p. 197401, 2013.
- [28] G. Zheng, H. Mühlenbernd, M. Kenney, G. Li, T. Zentgraf, and S. Zhang, "Metasurface holograms reaching 80% efficiency," *Nat. Nanotechnol.*, vol. 10, no. 4, pp. 308–312, 2015.
- [29] O. Quevedo-Teruel *et al.*, "Roadmap on metasurfaces," *J. Opt.*, vol. 21, no. 7, 2019, Art. no. 073002.
- [30] T. Matsui, S. Yamashita, H. Wado, H. Fujikawa, and H. Iizuka, "Flat grating lens utilizing widely variable transmission-phase via guided-modes," *Opt. Lett.*, vol. 40, no. 1, pp. 25–28, 2015.
- [31] Z. Wu, Y. Rafdi, and A. Grbic, "Tunable metasurfaces: A polarization rotator design," *Phys. Rev. X*, vol. 9, no. 1, 2019 Art. no. 011036.
- [32] J. B. Mueller, N. A. Rubin, R. C. Devlin, B. Groever, and F. Capasso, "Metasurface polarization optics: Independent phase control of arbitrary orthogonal states of polarization," *Phys. Rev. Lett.*, vol. 118, no. 11, p. 113901, 2017.
- [33] A. Arbabi, Y. Horie, M. Bagheri, and A. Faraon, "Dielectric metasurfaces for complete control of phase and polarization with subwavelength spatial resolution and high transmission," *Nat. Nanotechnol.*, vol. 10, no. 11, pp. 937–943, 2015.
- [34] H. Yang *et al.*, "A 1-bit  $10 \times 10$  reconfigurable reflectarray antenna: Design, optimization, and experiment," *IEEE Trans. Antennas Propag.*, vol. 64, no. 6, pp. 2246–2254, Jun. 2016.
- [35] A. M. Shaltout, V. M. Shalae, and M. L. Brongersma, "Spatiotemporal light control with active metasurfaces," *Science*, vol. 364, no. 6441, 2019.
- [36] X. G. Zhang *et al.*, "An optically driven digital metasurface for programming electromagnetic functions," *Nat. Electron.*, vol. 3, no. 3, pp. 165–171, 2020.
- [37] L. Dai *et al.*, "Reconfigurable intelligent surface-based wireless communications: Antenna design, prototyping, and experimental results," *IEEE Access*, vol. 8, pp. 45 913–45 923, 2020.
- [38] L. Zhang *et al.*, "Space-time-coding digital metasurfaces," *Nat. Commun.*, vol. 9, no. 1, pp. 1–11, 2018.
- [39] H. Yang *et al.*, "A programmable metasurface with dynamic polarization, scattering and focusing control," *Sci. Rep.*, vol. 6, p. 35692, 2016.
- [40] B. O. Zhu, J. Zhao, and Y. Feng, "Active impedance metasurface with full 360 reflection phase tuning," *Sci. Rep.*, vol. 3, p. 3059, 2013.
- [41] C.-F. Yang, B.-C. Wu, and C.-J. Ko, "A ray-tracing method for modeling indoor wave propagation and penetration," *IEEE Trans. Antennas Propag.*, vol. 46, no. 6, pp. 907–919, Jun. 1998.
- [42] J. R. James and P. S. Hall, *Handbook of Microstrip Antennas*, vol. 1, London, U.K.: Peter Peregrinus Ltd., 1989.
- [43] L. Zhu, P. Wecowski, and K. Wu, "New planar dual-mode filter using cross-slotted patch resonator for simultaneous size and loss reduction," *IEEE Trans. Microw. Theory Techn.*, vol. 47, no. 5, pp. 650–654, May 1999.
- [44] S. Sugiura and H. Iizuka, "Reactively steered ring antenna array for automotive application," *IEEE Trans. Antennas Propag.*, vol. 55, no. 7, pp. 1902–1908, Jul. 2007.
- [45] R. R. Mansour, "Design of superconductive multiplexers using single-mode and dual-mode filters," *IEEE Trans. Microw. Theory Techn.*, vol. 42, no. 7, pp. 1411–1418, Jul. 1994.
- [46] Simulia, "Dassault systems, CST microwave studio," 2017. [Online]. Available: <http://www.cst.com/>
- [47] Z. He and X. Yuan, "Cascaded channel estimation for large intelligent metasurface assisted massive MIMO," *IEEE Wireless Commun. Lett.*, vol. 9, no. 2, pp. 210–214, Feb. 2020.
- [48] D. C. Liu and J. Nocedal, "On the limited memory BFGS method for large scale optimization," *Math. Program.*, vol. 45, no. 1–3, pp. 503–528, 1989.
- [49] S. Sugiura, N. Suzuki, and H. Iizuka, "Effect of number of elements of a reactively loaded ring antenna array on the performance of beamwidth variation," *IEEE Antennas Wireless Propag. Lett.*, vol. 7, pp. 669–672, Mar. 2008.



**Shinya Sugiura** (Senior Member, IEEE) received the B.S. and M.S. degrees in aeronautics and astronautics from Kyoto University, Kyoto, Japan, in 2002 and 2004, respectively, and the Ph.D. degree in electronics and electrical engineering from the University of Southampton, Southampton, U.K., in 2010.

From 2004 to 2012, he was a Research Scientist with Toyota Central Research and Development Laboratories, Inc., Aichi, Japan. From 2013 to 2018, he was an Associate Professor with the Department of Computer and Information Sciences, Tokyo University of Agriculture and Technology, Koganei, Japan. Since 2018, he has been an Associate Professor with the Institute of Industrial Science, The University of Tokyo, Tokyo, Japan, where he heads the Wireless Communications Research Group. In 2019, he was recognized as The University of Tokyo Excellent Young Researcher. He is currently appointed as a PRESTO Researcher with the Japan Science and Technology Agency. He has authored or coauthored more than 80 IEEE journal papers. His research interests include wireless communications, networking, signal processing, and antenna technology.

He was the recipient of numerous awards including the Fifth Yasuharu Suematsu Award in 2019, the Sixth RIEC Award from the Foundation for the Promotion of Electrical Communication in 2016, the Young Scientists' Prize by the Minister of Education, Culture, Sports, Science and Technology of Japan in 2016, the 14th Funai Information Technology Award (First Prize) from the Funai Foundation in 2015, the 28th Telecom System Technology Award from the Telecommunications Advancement Foundation in 2013, the Sixth IEEE Communications Society Asia-Pacific Outstanding Young Researcher Award in 2011, the 13th Ericsson Young Scientist Award in 2011, and the 2008 IEEE Antennas and Propagation Society Japan Chapter Young Engineer Award. He was also certified as an Exemplary Reviewer of the IEEE COMMUNICATIONS LETTERS in 2013 and 2014 and the IEEE TRANSACTIONS ON COMMUNICATIONS in 2018. He is currently the Editor of the IEEE WIRELESS COMMUNICATIONS LETTERS.



**Yuto Kawai** received the B.S. degree in 2020 in electronic engineering from The University of Tokyo, Tokyo, Japan, where he is currently working toward the M.S. degree in information and communication engineering. His current research interests include intelligent reflecting surface and optimization of communications networks.



**Takayuki Matsui** received the B.S. and M.S. degrees in applied chemistry from Tohoku University, Sendai, Japan, in 2003 and 2005, respectively, and the Doctorate degree in engineering from Osaka University, Osaka, Japan, in 2015. In 2005, he was with Toyota Central R&D Labs., Inc., Nagakute, Japan. From 2015 to 2017, he was a Visiting Researcher with the Imperial College London, London, U. K. His research interests include nanophotonics, metasurfaces, and general optics.



**Taehwa Lee** (Member, IEEE) received the B.S. degree in mechanical engineering from Hanyang University, Seoul, South Korea, in 2007, the M.S. degree in mechanical engineering from the Pohang University of Science and Technology, Pohang, South Korea, in 2009, and the Doctorate degree in mechanical engineering from the University of Michigan, Ann Arbor, MI, USA, in 2015. Before moving to USA, from 2009 to 2011, he was an Assistant Manager with Samsung Heavy Industry, Inc., South Korea. After completing his Ph.D. degree, from 2016 to 2017,

he was a Postdoctoral Research Associate with Stanford University, Stanford, CA, USA. In 2017, he was with the Toyota Research Institute of North America, Toyota Motor North America, Inc., Ann Arbor, MI, USA. His research interests include wave-matter interaction in electromagnetics and acoustics.



**Hideo Iizuka** (Member, IEEE) received the B.S. and M.S. degrees in electrical engineering from Saitama University, Saitama, Japan, in 1995 and 1997, respectively, and the Doctorate degree in engineering from the Nagoya Institute of Technology, Nagoya, Japan, in 2007. In 1997, he was with Toyota Central R&D Labs., Inc., Nagakute, Japan. From 2001 to 2002, he was a Visiting Scholar with the University of Birmingham, Birmingham, U.K. From 2008 to 2011 and since 2017, he has been with the Toyota Research Institute of North America, Toyota Motor

North America, Inc., Ann Arbor, MI, USA. His research interests include analyses and developments of devices and sub-systems in electromagnetics and acoustics.